analytical chemistry

pubs.acs.org/ac

Article

Simultaneous Detection of Zinc and Its Pathway Metabolites Using MALDI MS Imaging of Prostate Tissue

Maria K. Andersen,* Sebastian Krossa, Therese S. Høiem, Rebecca Buchholz, Britt S. R. Claes, Benjamin Balluff, Shane R. Ellis, Elin Richardsen, Helena Bertilsson, Ron M. A. Heeren, Tone F. Bathen, Uwe Karst, Guro F. Giskeødegård, and May-Britt Tessem*

Cite This: *Anal. Chem.* 2020, 92, 3171−3179

Read Online

ACCESS | Metrics & More | Article Recommendations | Supporting Information

ABSTRACT: Levels of zinc, along with its mechanistically related metabolites citrate and aspartate, are widely reported as reduced in prostate cancer compared to healthy tissue and are therefore pointed out as potential cancer biomarkers. Previously, it has only been possible to analyze zinc and metabolites by separate detection methods. Through matrix-assisted laser desorption/ionization mass spectrometry imaging (MSI), we were for the first time able to demonstrate, in two different sample sets (n = 45 and n = 4), the simultaneous spatial detection of zinc, in the form of $ZnCl_3^-$, together with citrate, aspartate, and *N*-acetylaspartate on human prostate cancer tissues. The reliability of the $ZnCl_3^-$ detection was validated by total zinc determination using laser ablation inductively coupled plasma MSI on adjacent serial tissue sections. Zinc, citrate, and aspartate were correlated with each other (range r = 0.46 to 0.74) and showed a significant reduction in cancer compared to non-cancer epithelium ($p < 0.05$, $\log_2$ fold change range: −0.423 to −0.987), while no significant difference between cancer and stroma tissue was found. Simultaneous spatial detection of zinc and its metabolites is not only a valuable tool for analyzing the role of zinc in prostate metabolism but might also provide a fast and simple method to detect zinc, citrate, and aspartate levels as a biomarker signature for prostate cancer diagnostics and prognostics.

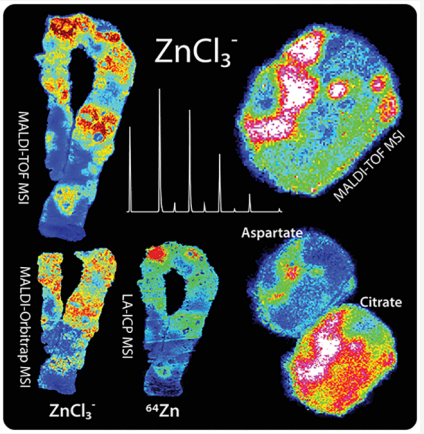

Healthy prostatic epithelial cells have a unique metabolism, with an extraordinary high production and secretion of the metabolite citrate and a very high zinc concentration.[1] Citrate production is facilitated through zinc mediated inhibition of aconitase. This enzyme is responsible for converting citrate to isocitrate in the tricarboxylic acid (TCA) cycle, and inhibition causes citrate accumulation[1] (Figure 1). It is proposed that imported aspartate serves as one of the main carbon sources for citrate, by conversion through oxaloacetate.[2] Aspartate can also be created from or converted to *N*-acetylaspartate (NAA),[3] but this potential mechanism is less investigated in prostate cells. Altered metabolism is one of the key characteristics of prostate cancer,[4] and during the course of cancer development, both citrate and zinc levels are reduced compared to healthy prostatic tissue and are therefore proposed as prostate cancer biomarkers.[1,5−7]

Detection of zinc in human prostate tissue has previously been performed by methods such as atomic absorption spectrometry,[8] X-ray fluorescent spectrometry,[6] inductively coupled plasma mass spectrometry (ICP-MS),[9] and zinc-specific fluorescent staining of tissue sections.[7,10] Laser ablation (LA) ICP MS imaging (MSI) has additionally been used to image zinc distribution in mouse brain tissue,[11] breast cancer,[12] and prostate cancer tissue.[13] Even though these are robust methods for zinc detection, they do not allow for the simultaneous detection of other biomolecules such as metabolites and lipids. Hence, studies of the zinc−citrate−aspartate pathway have until now required the use of different methods on different pieces of tissue. Matrix-assisted laser/desorption ionization (MALDI) MSI is a method suitable for spatial detection of a number of different metabolites and lipids and is becoming popular for analysis of heterogeneous cancer tissue.[14] Hou et al. demonstrated detection of zinc, among other metal ions, using MALDI, but did not detect zinc in human urine or blood samples nor mouse brain tissue sections.[15] However, as the zinc content in prostate is uniquely high compared to other tissues and biofluids,[1] MALDI MSI may be a suitable method to detect zinc in prostate tissue.

In this study, we demonstrate the use of MALDI time-of-flight (TOF) MSI for simultaneous spatial detection of zinc (in the form of $ZnCl_3^-$) and the relevant metabolites citrate,

Received: October 27, 2019
Accepted: January 16, 2020
Published: January 16, 2020

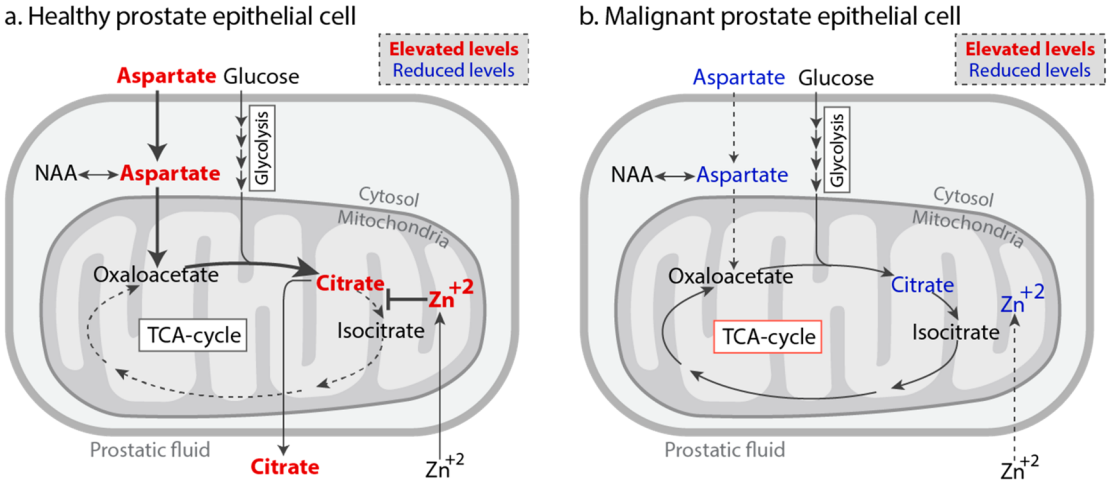

Figure 1. Metabolic alterations in prostate cancer as a consequence of reduced zinc levels. (a) In healthy prostate epithelial cells, a high intake of zinc inhibits the conversion of citrate to isocitrate, causing accumulation of citrate. Increased aspartate intake functions as a carbon source for citrate production. (b) In malignant prostate epithelial cells, reduced levels of zinc lead to citrate being utilized further into the TCA cycle. Abbreviation: NAA = *N*-acetylaspartate.

aspartate, and NAA in prostate cancer tissue sections. Comparing MALDI-TOF measured $ZnCl_3^-$ to total zinc concentration detected with LA-ICP-MS confirmed that $ZnCl_3^-$ is representative of the total zinc concentration in the tissue. This is the first time zinc has been detected together with other relevant metabolites in this important prostate cancer pathway through the exact same measurement.

MATERIAL AND METHODS

Sample Collection and Preparation. This study was approved by the Regional Committee for Medical Health and Research Ethics of Mid-Norway (identifier 2017/576), and all procedures followed national and EU ethical regulations. All patient donors signed an informed written consent before the tissue samples were collected.

Samples included in this study were fresh frozen prostate samples collected after radical prostatectomy of confirmed malignant prostates and stored at either −80 °C or in liquid nitrogen. Two different types of samples were used; the "*core samples*" (n = 45 samples, N = 15 patients) were disc-shaped samples (height 2 mm, Ø 3 mm) collected as described by Bertilsson et al.[16] from 2 mm thick frozen tissue slices. The "*biopsy samples*" (n = 4 samples, N = 4 patients) were collected with biopsy needles and were further embedded in 5% carboxymethyl cellulose (CMC) and 10% gelatin as described by Nelson et al.[17] All samples to be analyzed by MALDI MSI were cryosectioned at 4 μm and mounted onto indium tin oxide (ITO) covered glass slides (Bruker Daltonics, part nr. 9237001, Bremen, Germany). Three of the *core samples* and one of the *biopsy samples* were resectioned at a later point to produce several adjacent tissue sections, the validation sample sets, for additional experiments including LA-ICP MSI, remeasurement with MALDI-TOF MSI, and MALDI-Orbitrap. Tissue sections to be measured with LA-ICP MSI were cut at 10 μm and mounted onto regular light microscope glass slides. An overview of the methodological workflow is presented in Figure 2. All sections were stored at −80 °C until further use.

All tissue sections were vacuum-dried (>30 min) prior to data acquisition, and sections prepared for MALDI MSI

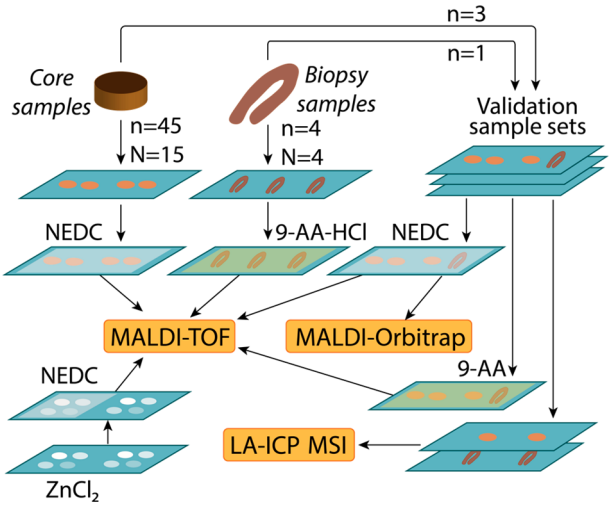

Figure 2. Workflow overview. Two fresh frozen prostate cancer sample sets, the *core samples* and the *biopsy samples*, were cryosectioned, mounted onto indium tin oxide (ITO) covered glass slides, and covered with *N*-(1-naphthyl) ethylenediamine dihydrochloride (NEDC) and 9-aminoacridine (9-AA) hydrochloride monohydrate (HCl) matrixes, respectively. Both sample sets were measured with MALDI-TOF MSI. Three of the *core samples* and one *biopsy sample* were sectioned for validation analysis, including remeasurement with MALDI-TOF MSI using NEDC matrix, MALDI-TOF MSI with chloride-free 9-AA matrix, high-mass-resolution MALDI-Orbitrap, and total zinc detection with LA-ICP MSI. Standards of $ZnCl_2$ were also measured with MALDI-TOF.

experiments were covered with matrix. As both sample sets used in this study originally were separate pilot experiments, two different matrix application methods were used. For the *core samples*, the TM-Sprayer M3 (HTX Technologies LLC, Carrboro, USA) was used to apply 14 layers of 7 mg/mL *N*-(1-naphthyl) ethylenediamine dihydrochlorid (NEDC) (Sigma-Aldrich, Gillingham, UK) dissolved in 70% methanol. The *biopsy samples* were covered with eight layers of 10 mg/mL of 9-aminoacridine hydrochloride monohydrate (9-AA HCl H_2O) (Sigma-Aldrich) mixed in 70% methanol, applied with SunCollect (SunChrom, Friedrichsdorf, Germany). It was

https://dx.doi.org/10.1021/acs.analchem.9b04903
Anal. Chem. 2020, 92, 3171−3179

suspected that the available chloride ions present in both matrixes used could contribute to the formation of $ZnCl_3^-$. To investigate this potential effect, one of the validation sample sets was covered with 9-AA without hydrochloride monohydrate (9-AA) (Sigma-Aldrich), using the same concentration and spraying parameters as for 9-AA HCl H_2O. Exact spraying parameters for all matrices are presented in Supplementary Table S1.

MALDI MSI Data Acquisition. MALDI-TOF MSI was performed on all samples using a rapifleX MALDI-TOF Tissuetyper (Bruker Daltonics) operating in reflector negative ion mode across a mass range of m/z 40−1000, acquiring 200 shots per pixel at a 10 kHz frequency. The *core samples* and the *biopsy samples* were measured with pixel sizes of 30 and 50 μm, respectively. The rapifleX instrument was calibrated using red phosphorus clusters before each measurement. After MALDI measurements, all tissue sections were stained with hematoxylin and eosin (H&E), digitally scanned with the Mirax digital slide scanning system (Zeiss, Jana, Germany), and evaluated through histology by an experienced uropathologist.

To verify that $ZnCl_3^-$ can be created from zinc and chloride ions by the MALDI-TOF process, $ZnCl_2$ standards (Sigma-Aldrich) were also measured by the rapifleX instrument. $ZnCl_2$ was dissolved in 100% ethanol to produce concentrations of 1, 2.5, 5, and 10 mg/mL, and 1 μL of each solution was placed on ITO glass slides and left to dry. MALDI-TOF measurements were performed both on $ZnCl_2$ standards covered with NEDC matrix (same parameters as previously described) and uncovered $ZnCl_2$ standards.

High-mass-resolution acquisition and tandem MS for identification of citrate, aspartate, and NAA were performed on the MALDI-Orbitrap system Q Exactive HF Hybrid Quadrupole (Thermo Fisher Scientific GmbH, Bremen, Germany) coupled to a MALDI/ESI injector (Spectroglyph LLC, Kennewick, WA, USA). Tandem MS was performed using a higher-energy collisional dissociation cell with an isolation window of ±0.5 Da, a normalized collision energy in the range of 20−65 (manufacturer units), a laser shot frequency of 1000 Hz, and a mass resolution of 240 000 (fwhm at m/z 200). For each precursor, 20 spectra were acquired using an injection time of 2000 ms per scan while continuously moving the stage. Additionally, imaging measurements were performed using MALDI-Orbitrap (m/z 160−180, spatial resolution 30 μm, 1000 Hz laser frequency, and 550 ms injection time) in negative ion mode in order to identify masses that may be overlapping with the isotopic $ZnCl_3^-$ masses in the MALDI-TOF experiments. Measurements of two *core sample* sections had to be disregarded due to a problem with the ion transmission of the source, leaving us with imaging data of one *core sample* and one *biopsy sample*. All MALDI-Orbitrap measurements were performed on samples covered with NEDC matrix according to the previously described spraying method.

LA-ICP MSI Experiments. To validate that the spatial detection of $ZnCl_3^-$ with MALDI is representative of total zinc distribution in the tissue, LA-ICP MSI for total zinc detection was performed on adjacent tissue sections from those of MALDI-TOF MSI measurements. The tissue samples were analyzed at a spatial resolution of 15 μm with an ICPMS-2030 instrument (Shimadzu, Kyoto, Japan) coupled to the laser ablation system, LSX-213 G2+ (Teledyne Cetac, Omaha, USA). Samples were ablated via line-by-line scan with a pixel size of 15 μm, a scan speed of 45 μm/s, and 800 mL/min He as transport gas. The analysis was performed in collision gas mode with He as collision gas. Integration times for ^{64}Zn and ^{66}Zn were 75 ms. For the quantification of Zn, matrix-matched standards based on gelatin were used. Eight gelatin standards (10% w/w) including a blank were spiked with different Zn concentrations ranging from 1 to 500 μg/g. A separate test tissue section placed on the same glass slide was used to optimize the ablation process for each measurement.

Data Preprocessing. FlexImaging v4.1 (Bruker Daltonics) was used to coregister the H&E stained and scanned histology images to the MALDI-TOF MSI measurements. In this software, the histopathology annotations for the *core samples* were used to define regions of interest (ROI): non-cancer epithelium, stroma, and cancer. In cases of less successful histology coregistrations (evident by shifts in histology images compared to on-tissue measurements), an in-house R-script was used to adjust the X and Y-coordinates of the ROIs in the mis file (flexImaging specific file) to fit the MSI measurement (Supplementary Script S1). All *core samples* measurements were combined using SCiLS Lab 2016b (SCiLS GmbH, Bremen Germany) with a convolution baseline subtraction (width: 75). Each spectrum was normalized by its total ion count. For the *core samples*, the acquired single spectra were organized into either non-cancer epithelium, stroma, or cancer, according to the histology annotations and exported as CSV files. An in-house R-script (Supplementary Script S2) was used to extract the peak intensity of aspartate (m/z 132.02), NAA (m/z 174.04), citrate (m/z 191.02), and the isotopic peaks of $ZnCl_3^-$ (m/z 168.84, 170.83, 171.83, 172.83, 173.82 174.82, 175.82, 176.82, 177.82, and 178.82). Peak intensity was defined as the highest point of a peak. Thermo Xcalibur 3.0.28 (Thermo Fisher Scientific, Bremen, Germany) was used to analyze the MALDI-Orbitrap imaging measurements. For visualization, the imaging data was converted to mzXML format using RawConverter[18] and analyzed using an in-house built MATLAB GUI.[19,20]

The metabolites aspartate, NAA, and citrate were identified through comparing the tandem MS spectra to the theoretical or validated measured fragment spectra in databases, including METLIN (https://metlin.scripps.edu)[21] and the Human Metabolome Database (http://www.hmdb.ca/).[22]

Statistical Analysis. Pearson statistics in R were used to calculate the match between the measured and theoretical $ZnCl_3^-$ isotopic peak patterns and to investigate the spatial relation between zinc and the metabolites aspartate and citrate. The theoretical isotopic pattern of $ZnCl_3^-$ was obtained from ChemCalc.org[23] with the mass resolution comparable to both the MALDI-TOF and MALDI-Orbitrap measurement, 3000 and 240 000 fwhm, respectively. The corr.test function from the *psych* package[24] was used to calculate the correlation between the analytes, and the correlation plots were created with the package *corrplot*.[25] For all correlation analyses, significance was calculated in R by t-tests and defined as $p < 0.05$.

To investigate the biological association between zinc, citrate, aspartate, and NAA, and the different tissue components (non-cancer epithelium, stroma, and cancer), univariate linear mixed models (LMM) were performed in R with the *nlme* v3.1-137 package[26] (Supplementary Script S3). LMM was used in order to include patient origin as a random effect. Due to overlapping masses for some of the isotopic peaks of $ZnCl_3^-$, the m/z 174.82 mass was used to represent zinc, as this would exclude any interference from other masses.

https://dx.doi.org/10.1021/acs.analchem.9b04903
Anal. Chem. 2020, 92, 3171−3179

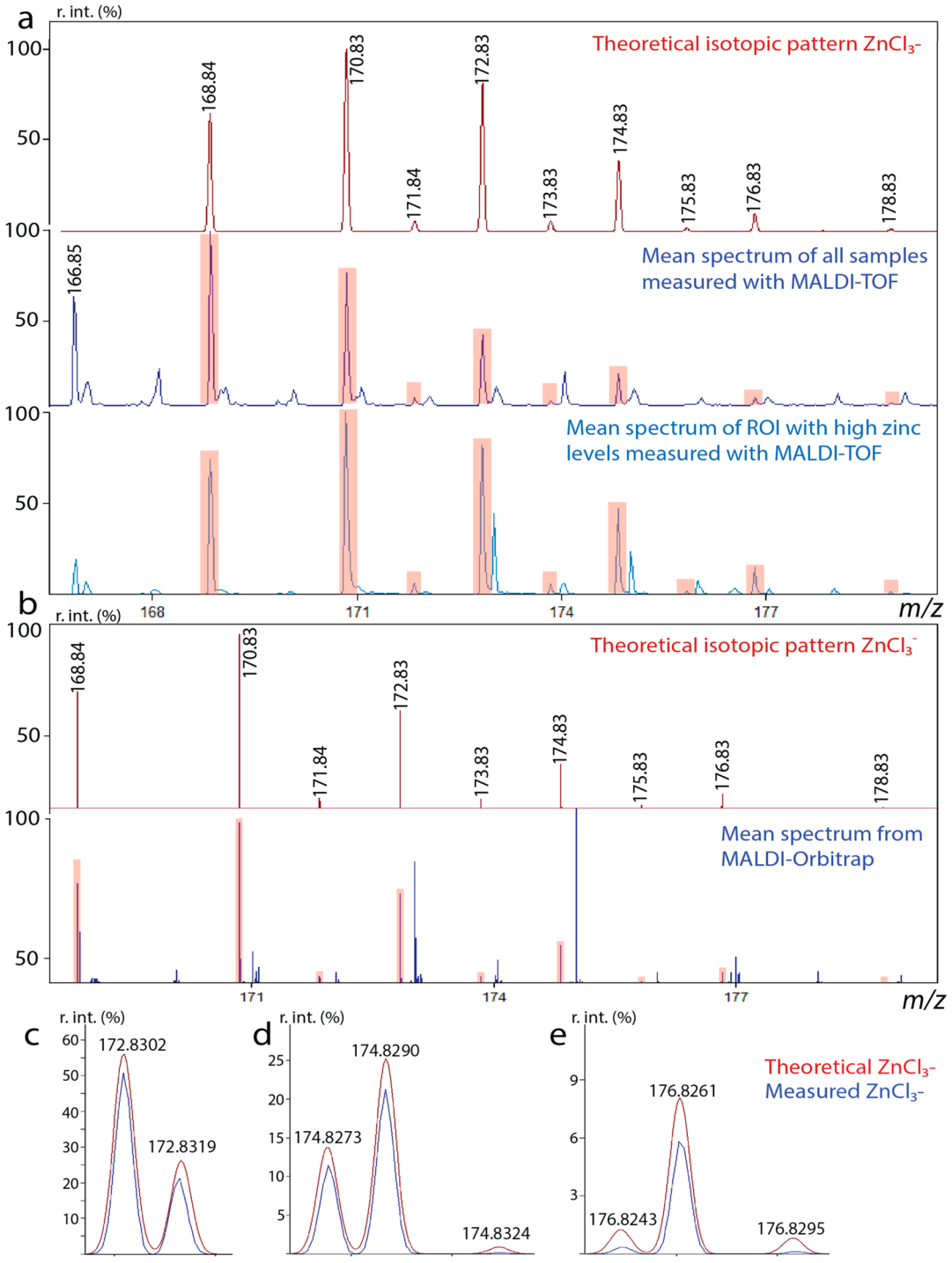

Figure 3. Measured isotopic peak pattern compared to theoretical pattern of zinc trichloride ($ZnCl_3^-$). (a) The theoretical isotopic peak pattern of $ZnCl_3^-$ (top spectrum, fwhm = 3000, from ChemCalc.org[23]) was compared to the mean spectrum measured by MALDI-TOF MSI acquisition (middle spectrum). Due to a contaminating molecule (m/z 166.85) likely to have interfering isotopic masses, a mean spectrum was created from selected regions of interest (ROI) with high $ZnCl_3^-$ contents. This high-$ZnCl_3^-$ spectrum proved to be very similar to the theoretical spectrum. (b) A separate measurement using high-mass-resolution MALDI-Orbitrap (bottom spectrum) was also compared to the theoretical isotopic peak pattern (fwhm = 240 000, ChemCalc.org) and additionally showed (c–e) a matching isotopic fine structure. Transparent red indicates detected $ZnCl_3^-$ isotopic peaks. Abbreviation: r. int. = relative intensity.

LMM was performed by randomly selecting 0.5% of the spectra to build models. This strategy was used to limit the effect of spatial autocorrelation, common to MSI data.[27] Choosing a fraction of 0.5% limits the average number of neighboring pixels selected to approximately 3.9%, according to probability statistics ($P(A_1 \cup A_2 \ldots \cup A_8) = 1 - 0.995^8$, where A_{1-8} are neighboring pixels). This fraction based LMM was repeated 1000 times for each mass for each pairwise comparison, and the mean p-value and $\log_2$ fold change ($\log_2$FC) were calculated. A p-value below 0.05 was considered significant. For LMM models to be valid, the residuals need to be normally distributed. An automatized strategy was used to

https://dx.doi.org/10.1021/acs.analchem.9b04903
Anal. Chem. 2020, 92, 3171−3179

assess normality for each model (described in Supplementary Text S1). In cases where the models failed the normality assumption, the peak intensity levels were log transformed, and a new LMM model was calculated. A second normality fail would cause exclusion of that iteration.

RESULTS AND DISCUSSION

Zinc Can Be Detected with MALDI MSI in Prostate Tissue. $ZnCl_3^-$ was initially discovered in our prostate *core samples* MALDI-TOF MSI data set (n = 45), by manual untargeted spectral and spatial mass distribution evaluation. We found that the m/z 168.84 mass had a similar spatial distribution (Supplementary Figure S1) to eight other ions with higher m/z values approximately 1 or 2 Da apart (m/z 170.83, 171.83, 172.83, 173.82, 174.82, 175.82, 176.82, 177.82, and 178.82). This strongly suggested that the nine masses were isotopic peaks representing the same compound. Based on the mass defect and isotope pattern, the ions were assumed to belong to an inorganic molecule. Searching in METLIN[21] for the monoisotopic mass (m/z 168.84) gave $ZnCl_3^-$ as a possible identity. Further investigating the isotopic peak pattern of $ZnCl_3^-$ confirmed that the nine masses represented the different combinations of stable isotopes of zinc (^{64}Zn, ^{66}Zn, ^{67}Zn, and ^{68}Zn) and chloride (^{35}Cl and ^{37}Cl). However, according to the theoretical isotopic spectrum (Figure 3a, top spectrum), the second mass (m/z 170.83) should be the most abundant mass, while the mean spectrum from our data set (Figure 3a and Supplementary Data) indicated the monoisotopic m/z 168.84 mass to be the most abundant. A lower mass of m/z 166.85 was suspected to interfere by having isotopic masses overlapping with some of the $ZnCl_3^-$ isotopic peaks. Further investigation revealed the m/z 166.85 mass to be tetrachloroaluminate ($AlCl_4^-$) as presented in Supplementary Text S2 and Supplementary Figures S5–S7. By creating a new mean spectrum with five different ROIs that had high $ZnCl_3^-$ levels (Figure 3a and Supplementary Data), thereby minimizing the interference from m/z 166.85, a spectrum more similar to the theoretical spectrum was produced. This high-zinc-level spectrum had a significantly high correlation with the theoretical spectrum of $ZnCl_3^-$ (r = 0.996, $p = 1.92 \times 10^{-8}$). This initial discovery was based on analysis of NEDC matrix covered tissue samples. A second smaller sample set, consisting of CMC and gelatin embedded *biopsy samples* (n = 4) covered with 9-AA matrix, did also show detection of the $ZnCl_3^-$ isotopic peaks (Supplementary Figure S2). This demonstrates that $ZnCl_3^-$ can be detected in prostate tissue with different matrices and using different sample processing methods.

To our knowledge, this is the first reported $ZnCl_3^-$ detection in any tissue sample. $ZnCl_3^-$ has previously been reported as a side-product in chemical reactions using MS methods.[28−30] Hou et al. demonstrated detection of $ZnCl_3^-$ using MALDI-TOF with NEDC matrix in solutions of $ZnCl_2$ and in samples of lake water but could not detect $ZnCl_3^-$ in biological samples such as urine and plasma.[15] At this point, a likely explanation is that $ZnCl_3^-$ forms in the MALDI process through tissue-specific zinc (from salts or biological complexes) that pairs up with excess chloride ions. We first hypothesized that the excess chloride ions may originate from the NEDC matrix, which is applied as a solution of its hydrochloride salt. Using MALDI-TOF on $ZnCl_2$ standards, both with and without NEDC matrix, confirms that $ZnCl_3^-$ can be created from $ZnCl_2$ alone in the MALDI process (Supplementary Figure S3). We further performed MALDI-TOF measurements using chloride-free 9-AA matrix on prostate tissue and were still able to detect $ZnCl_3^-$ but at a lower sensitivity (Supplementary Figure S4). However, this matrix gave lower sensitivity for other masses as well (e.g., citrate was not detected), indicating a generally lower ionization efficiency of this matrix. Based on our own and others results that have successfully used NEDC for metal detection,[15] we would perform subsequent experiments using this matrix for $ZnCl_3^-$ detection.

In order to acquire accurate mass of $ZnCl_3^-$ and identify the contaminating peak of m/z 166.86 (Supplementary Text S2), an additional high-mass-resolution acquisition was performed using MALDI-Orbitrap. A total of 14 isotopic $ZnCl_3^-$ peaks were detected with a mass error of less than 2 ppm (Figure 3b and Supplementary Data). We were further able to separate the isotopic fine structure for the m/z 172.83, 174.83, and 176.83 masses (Figure 3c–e), which explains the higher number of detected isotopic peaks compared to MALDI-TOF. Similar to MALDI-TOF, the mean MALDI-Orbitrap spectrum of the detected $ZnCl_3^-$ masses had a high degree of correlation with the theoretical isotopic masses (r = 0.999, $p = 2.2 \times 10^{-16}$).

Spatial $ZnCl_3^-$ Distribution Matches Total Zinc Detection. LA-ICP MSI is a well-established method to quantitatively image total metal content, including total zinc, in prostate tissue.[13] Thus, to further verify the results from MALDI-TOF MSI, we performed LA-ICP MSI on an adjacent serial tissue section for absolute quantification and distribution analysis of zinc (^{64}Zn). The aim was also to see if the distribution of $ZnCl_3^-$ is representative of total zinc distribution. From visual assessment, there is a general agreement between the spatial distribution of $ZnCl_3^-$ and total zinc detected with MALDI-TOF MSI and LA-ICP MSI, respectively (Figure 4 and Supplementary Figure S8). We note that non-optimal tissue integrity for some of the validation samples made the match between sections measured with LA-ICP MSI and MALDI-TOF MSI less apparent (see Supplementary Figure S8), although roughly the same areas of the sections show a similar zinc distribution. Additionally, when comparing to the stained histology sections, elevated levels of zinc are localized to non-cancer epithelial glands for both measurements. Overall, this adds further evidence that MALDI MSI can reliably be used for zinc detection.

Zinc Is Correlated to Citrate and Aspartate. In addition to being substantially faster, a major strength of using MALDI-TOF MSI for imaging zinc compared to LA-ICP MSI is that the former method is also capable of simultaneously detecting small metabolites that are closely biologically related to zinc. Two such metabolites are citrate and aspartate (Figure 1), which we detected in the exact same MALDI-TOF MSI measurements. Zinc ($ZnCl_3^-$, m/z 174.82) was significantly correlated with citrate (r = 0.64) and aspartate (r = 0.46), while citrate and aspartate had a stronger correlation with each other (r = 0.74, Figure 5a) ($p < 0.001$). The lower correlation between zinc and aspartate suggests that zinc is closely linked to citrate and is further away from aspartate in the metabolic pathway (Figure 1). Overall, our results further support the previous findings that high levels of zinc lead to high levels of citrate[1] and that aspartate is one of the key carbon sources for citrate production.[2] It should be noted that these findings are metabolic snapshots and do not prove the direct mechanistic association between zinc, citrate, and aspartate. However, the correlation analysis is based on more than 190 000 spectra, originating across 45 tissue samples with a range of different

https://dx.doi.org/10.1021/acs.analchem.9b04903
Anal. Chem. 2020, 92, 3171−3179

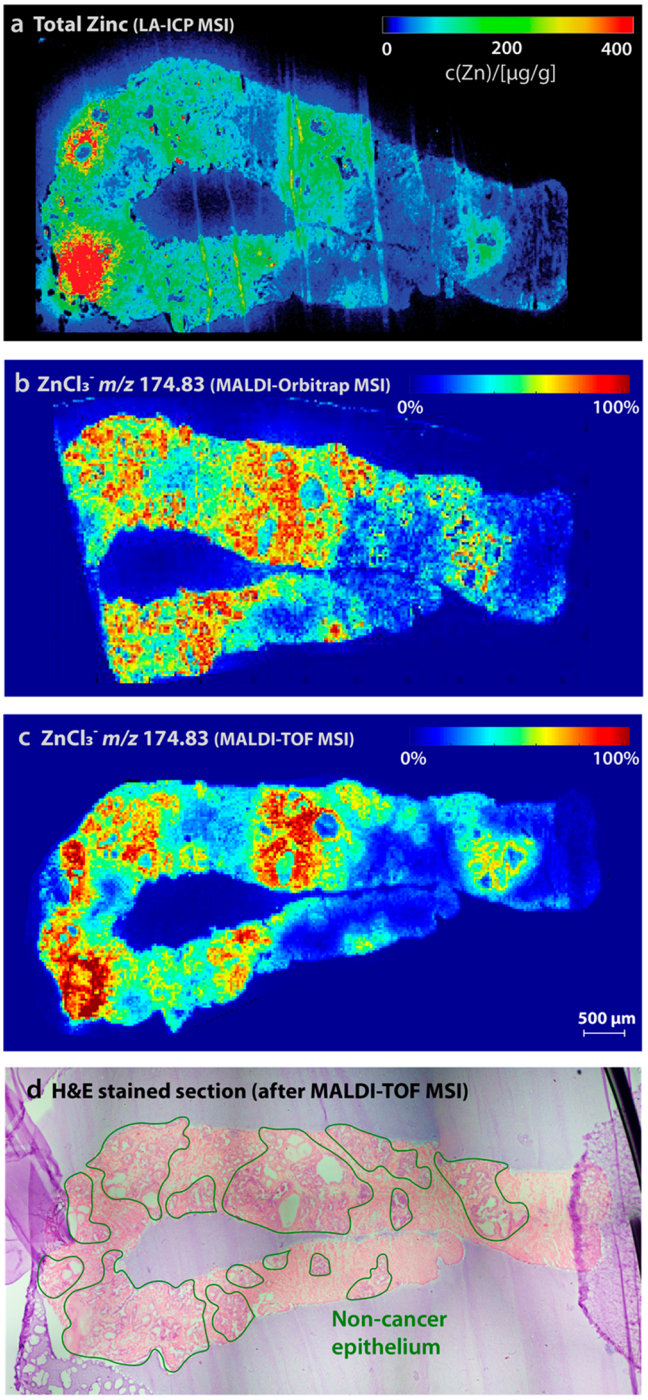

Figure 4. Heat maps comparing MALDI MSI to LA-ICP MSI for spatial zinc detection. (a) Total zinc detected with LA-ICP MSI had a matching spatial distribution with $ZnCl_3^-$ detected with both (b) MALDI-Orbitrap and (c) MALDI-TOF MSI. (d) Annotated histopathology of the sections used for MALDI-TOF MSI further showed that high zinc levels are located to non-cancer epithelium. A part of the section used for (b) MALDI-Orbitrap was lost during cryosectioning.

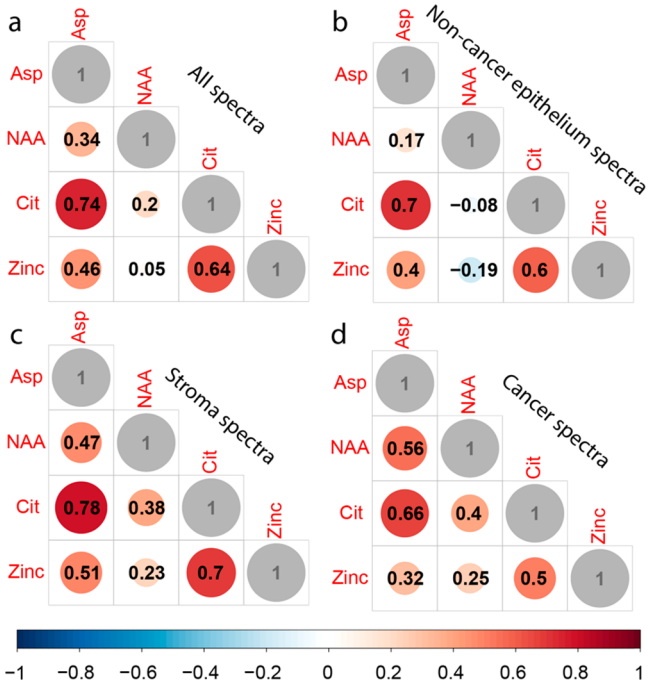

Figure 5. Correlation analysis of zinc and relevant metabolites. Pearson statistics were used to calculate correlation between zinc, citrate (Cit), aspartate (Asp), and *N*-acetylaspartate (NAA) for (a) all spectra, (b) non-cancer epithelium spectra, (c) stroma spectra, and (d) cancer spectra. The figure was made using the *corrplot* package[25] in R.

histology features, adding substantial confidence to the results. The spatial distribution of the masses used for correlation analysis on the *core samples* is presented in Supplementary Figure S9.

Performing separate correlation analysis on spectra from only non-cancer epithelium and from stroma still showed similar correlations between zinc, aspartate, and citrate (Figure 5b,c). However, in cancer, these correlations were lower (Figure 5d). This may indicate that the zinc−citrate−aspartate pathway mechanism present in healthy prostate epithelium gets more obstructed during prostate cancer development.

Currently, aspartate for citrate production is thought to be largely imported, based on the reported high level of the aspartate transporter in benign prostate epithelium.[31] Aspartate can also be synthesized inside the cell from NAA[3] (Figure 1), a reversible reaction. However, this mechanism has not been reported to be an important source of aspartate in healthy prostate epithelium. Interestingly, the correlation between NAA and aspartate in non-cancer epithelium is relatively low (r = 0.17), while a higher correlation is found in stroma and cancer (Figure 5b−d). The low correlation in non-cancer epithelium supports the current knowledge that aspartate in healthy prostate tissue may be predominantly imported to facilitate citrate production.[31] During cancer progression, import is halted, and aspartate may be more associated with conversion to/from NAA, causing an increased correlation. Further targeted functional studies are needed to accurately assess this proposed metabolic mechanism.

Significantly Reduced Levels of Zinc, Citrate, and Aspartate in Prostate Cancer Tissue. Pairwise univariate LMM and log_2FC showed that zinc, citrate, and aspartate were significantly reduced in cancer compared to non-cancer epithelium tissue (Table 1). Lower levels of zinc and citrate in prostate cancer were largely reported before[6−8,32] and have been linked to a worse clinical outcome.[5,9] However, this is the first time the spatial distribution of zinc has been shown on heterogeneous tissue sections using MALDI MSI (Figure 6). Zinc had a larger decrease than citrate and aspartate in cancer

https://dx.doi.org/10.1021/acs.analchem.9b04903
Anal. Chem. 2020, 92, 3171−3179

Table 1. Linear Mixed Models (LMM) and Log_2 Fold Change (log_2FC) Were Used To Investigate Differences in Levels of Zinc ($ZnCl_3^-$) and Relevant Metabolites, Citrate, Aspartate, and *N*-Acetylaspartate (NAA), across Non-Cancer Epithelium (NCE), Stroma, and Cancer Tissue Types

m/z	ID	NCE/stroma log_2FC	NCE/stroma adj *p*-value	cancer/NCE log_2FC	cancer/NCE adj *p*-value	cancer/stroma log_2FC	cancer/stroma adj *p*-value
132.03	aspartate	0.617	4.90×10^{-07}[a]	−0.423	0.00018[a]	0.197	0.5
174.04	NAA	0.311	0.32	0.849	0.14	1.169	0.024[a]
191.02	citrate	0.83	1.40×10^{-11}[a]	−0.695	0.00016[a]	0.138	0.41
174.82	$ZnCl_3^-$	0.789	7.70×10^{-06}[a]	−0.987	0.0019[a]	−0.197	0.39

[a]Significant *p*-value from univariate LMM.

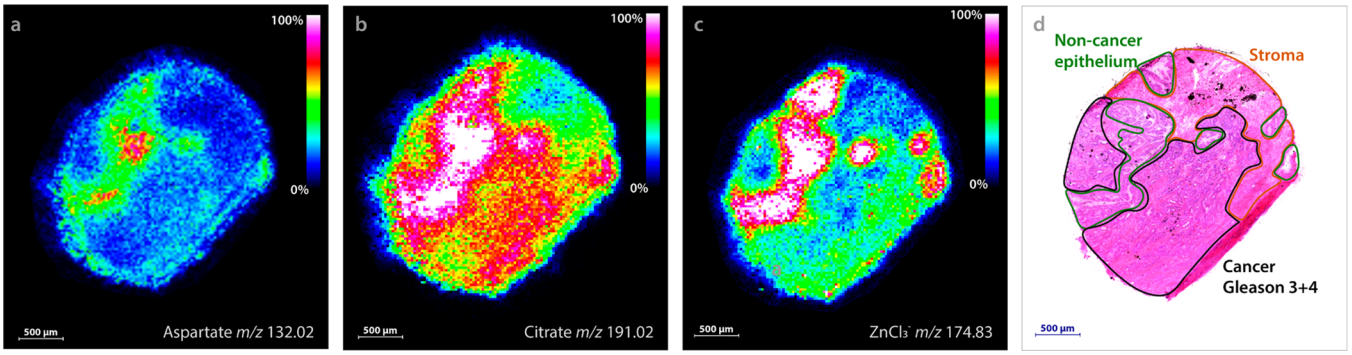

Figure 6. Comparison of the spatial distributions detected with MALDI-TOF MSI. (a) Aspartate and (b) citrate had a very similar spatial distribution with (c) zinc ($ZnCl_3^-$). (d) The spatial distributions of these three masses also matched to annotated non-cancer epithelium.

compared to non-cancer epithelium ($log_2FC = -0.99$, $p = 0.0019$) and was more spatially localized to non-cancer epithelial glands (Figure 6). This makes zinc a potential marker to aid the identification of glands that may be cancerous. It should be noted that the non-cancer epithelium regions used for analysis in this study came from malignant prostates and may not be considered truly healthy tissue. Due to ethical concerns, it is highly unusual to get access to normal and metabolically preserved prostate tissue from healthy men. Although this can limit elucidation of the full biological development of prostate cancer, it is more clinically relevant to differentiate cancerous glands from, for example, benign prostate hyperplasia, which is a highly common non-cancerous condition in older men.

Our results also show that stroma has comparable decreased levels of zinc, citrate, and aspartate to cancer tissue, demonstrating how stroma content in prostate tissue samples can confound whole-sample metabolic analysis of prostate samples, such as nuclear magnetic resonance spectroscopy (NMR) and liquid chromatography/MS (LC/MS). This pinpoints the value of methodology that maintains spatial information, especially in biomarker research based on analyzing heterogeneous cancer samples.

In contrast to zinc, citrate, and aspartate, NAA had higher levels in cancer compared to stroma ($log_2FC = 1.169$, $p = 0.024$) and a tendency of higher levels when compared to non-cancer epithelium although not significant ($log_2FC = 0.849$, $p = 0.14$). Elevated levels of NAA have previously been identified in ovarian,[33] lung,[34] and prostate cancer.[35] The specific role of NAA in cancer development remains unclear but may be related to increased lipid synthesis,[36] a well-established phenomenon of different cancer types, including prostate cancer.[37]

Implications of $ZnCl_3^-$ Detection with MALDI MSI. MALDI MSI is not generally recommended for detection of metals and metal containing molecules on tissue due to a low ionization efficiency.[38] It was therefore unexpected to identify $ZnCl_3^-$ in our data set. As reduced levels of zinc have been reported for a number of different cancers, including lung, breast, and liver,[39] investigating the potential detection of $ZnCl_3^-$ in other human tissues would be of interest. However, a very relevant underlying fact of our novel finding is that the prostate gland has an unusual high concentration of zinc, as much as 10−20-fold greater compared to other tissues.[1] Consequently, zinc detection with MALDI MSI on other tissues may be more challenging than prostate tissue due to substantial lower concentrations.

Due to the simultaneous detection of zinc ($ZnCl_3^-$) together with other relevant metabolites, we could successfully investigate these close metabolic relationships. Further research of the diagnostic and prognostic value of these molecular features detected with MALDI, both singularly and in combination, on a larger patient cohort, may reveal robust clinical biomarkers. Both zinc and citrate are previously proposed biomarkers, due to their systematic reduction in prostate cancer.[5−7,32,40] Importantly, simultaneous detection of these compounds in the same measurement without any additional experimental adjustments makes them more interesting as clinical biomarkers. MALDI-TOF MSI instrumentation, such as rapifleX, is additionally proposed as clinical tools due to its high speed, making rapid diagnostics possible.[41,42]

CONCLUSION

In this study, we have demonstrated the spatial detection of the cancer biomarker zinc, in the form of $ZnCl_3^-$, on prostate tissue using MALDI-TOF MSI. This method can detect a wide range of molecules, which enabled us to simultaneously detect the metabolically closely associated metabolites citrate, aspartate, and NAA. We identified clear biological associations between zinc, citrate, and aspartate, and tissue type, where all

https://dx.doi.org/10.1021/acs.analchem.9b04903
Anal. Chem. 2020, 92, 3171−3179

features were correlated with each other and were reduced in cancer compared to non-cancer epithelium. Simultaneous spatial detection of zinc and citrate, in particular, with MALDI-TOF MSI, may be a promising tool both for prostate cancer diagnosis and prognosis.

■ ASSOCIATED CONTENT

Supporting Information

The Supporting Information is available free of charge at https://pubs.acs.org/doi/10.1021/acs.analchem.9b04903.

Matrix spraying parameters, description of normality test, spatial distribution of $ZnCl_3^-$ isotopic peaks with MALDI-TOF MSI, MALDI-TOF MSI measurement of the biopsy samples, MALDI-TOF MSI measurement of $ZnCl_2$ standards, MALDI-TOF measurement using chloride-free 9-AA matrix, identification of tetrachloroaluminate ($AlCl_4^-$), spectral investigation of $AlCl_4^-$, detection of $AlCl_4^-$ on matrix-only regions, spatial distribution of *m/z* 166.85, comparing spatial distribution of total zinc and $ZnCl_3^-$, and spatial distribution of $ZnCl_3^-$ and metabolites (PDF)

Supplementary Script S1: Script to change ROI coordinates in a flexImaging mis file (TXT)

Supplementary Script S2: Function to select highest data point in a peak interval (TXT)

Supplementary Script S3: Function to perform linear mixed models (LMM) on a random selection of spectra from MALDI measurements (TXT)

Mean spectra from MALDI-TOF MSI acquisition of all *core samples*, MALDI-TOF MSI of ROI with high zinc levels, and MALDI-Orbitrap MSI (XLSX)

■ AUTHOR INFORMATION

Corresponding Authors

Maria K. Andersen − *Department of Circulation and Medical Imaging, Norwegian University of Science and Technology (NTNU), 7491 Trondheim, Norway;* orcid.org/0000-0003-2883-2450; Email: maria.k.andersen@ntnu.no

May-Britt Tessem − *Department of Circulation and Medical Imaging, Norwegian University of Science and Technology (NTNU), 7491 Trondheim, Norway; Clinic of Surgery, St. Olavs Hospital, Trondheim University Hospital, 7030 Trondheim, Norway*; Email: may-britt.tessem@ntnu.no

Authors

Sebastian Krossa − *Department of Circulation and Medical Imaging, Norwegian University of Science and Technology (NTNU), 7491 Trondheim, Norway*

Therese S. Høiem − *Department of Circulation and Medical Imaging, Norwegian University of Science and Technology (NTNU), 7491 Trondheim, Norway*

Rebecca Buchholz − *Institute of Inorganic and Analytical Chemistry, University of Münster, D-48149 Münster, Germany*

Britt S. R. Claes − *Maastricht MultiModal Molecular Imaging Institute (M4I), Maastricht University, 6229 ER Maastricht, The Netherlands*

Benjamin Balluff − *Maastricht MultiModal Molecular Imaging Institute (M4I), Maastricht University, 6229 ER Maastricht, The Netherlands*

Shane R. Ellis − *Maastricht MultiModal Molecular Imaging Institute (M4I), Maastricht University, 6229 ER Maastricht, The Netherlands;* orcid.org/0000-0002-3326-5991

Elin Richardsen − *Department of Medical Biology, The Arctic University of Norway (UIT), 9037 Tromsø, Norway; Department of Clinical Pathology, University Hospital of North Norway, UNN, 9019 Tromsø, Norway*

Helena Bertilsson − *Department of Clinical and Molecular Medicine, Norwegian University of Science and Technology (NTNU), 7491 Trondheim, Norway; Clinic of Surgery, St. Olavs Hospital, Trondheim University Hospital, 7030 Trondheim, Norway*

Ron M. A. Heeren − *Maastricht MultiModal Molecular Imaging Institute (M4I), Maastricht University, 6229 ER Maastricht, The Netherlands;* orcid.org/0000-0002-6533-7179

Tone F. Bathen − *Department of Circulation and Medical Imaging, Norwegian University of Science and Technology (NTNU), 7491 Trondheim, Norway*

Uwe Karst − *Institute of Inorganic and Analytical Chemistry, University of Münster, D-48149 Münster, Germany;* orcid.org/0000-0002-1774-6787

Guro F. Giskeødegård − *Department of Circulation and Medical Imaging, Norwegian University of Science and Technology (NTNU), 7491 Trondheim, Norway*

Complete contact information is available at: https://pubs.acs.org/10.1021/acs.analchem.9b04903

Notes

The authors declare no competing financial interest.

■ ACKNOWLEDGMENTS

This research was funded by the European Research Council (ERC) under the European Union's Horizon 2020 research and innovation program (grant agreement No. 758306), Norwegian University of Science and Technology (NTNU), Liaison Committee RHA-NTNU, Maastricht University, the LINK program of the Dutch province of Limburg, Norwegian Cancer Society, The Northern Health Administration, and UiT - The Arctic University of Norway. We thank Biobank1 (St. Olavs Hospital) for collecting and storing the *core sample* set. Sectioning of samples was performed by the cellular and molecular imaging core facility (CMIC) at NTNU

■ REFERENCES

(1) Costello, L. C.; Franklin, R. B. *Arch. Biochem. Biophys.* **2016**, *611*, 100−112.

(2) Costello, L. C.; Franklin, R. B. *Prostate* **1989**, *15* (4), 335−342.

(3) Wiame, E.; Tyteca, D.; Pierrot, N.; Collard, F.; Amyere, M.; Noel, G.; Desmedt, J.; Nassogne, M. C.; Vikkula, M.; Octave, J. N.; Vincent, M. F.; Courtoy, P. J.; Boltshauser, E.; van Schaftingen, E. *Biochem. J.* **2010**, *425* (1), 127−36.

(4) Eidelman, E.; Twum-Ampofo, J.; Ansari, J.; Siddiqui, M. M. *Front. Oncol.* **2017**, *7*, 131.

(5) Giskeødegård, G. F.; Bertilsson, H.; Selnæs, K. M.; Wright, A. J.; Bathen, T. F.; Viset, T.; Halgunset, J.; Angelsen, A.; Gribbestad, I. S.; Tessem, M.-B. *PLoS One* **2013**, *8* (4), No. e62375.

(6) Zaichick, V.; Sviridova, T. V.; Zaichick, S. V. *Int. Urol. Nephrol.* **1997**, *29* (5), 565−74.

(7) Johnson, L. A.; Kanak, M. A.; Kajdacsy-Balla, A.; Pestaner, J. P.; Bagasra, O. *Methods* **2010**, *52* (4), 316−21.

(8) Christudoss, P.; Selvakumar, R.; Fleming, J. J.; Gopalakrishnan, G. *Indian J. Urol.* **2011**, *27* (1), 14−8.

(9) Sarafanov, A. G.; Todorov, T. I.; Centeno, J. A.; Macias, V.; Gao, W.; Liang, W. M.; Beam, C.; Gray, M. A.; Kajdacsy-Balla, A. A. *Prostate* **2011**, *71* (11), 1231−8.

(10) Franklin, R. B.; Feng, P.; Milon, B.; Desouki, M. M.; Singh, K. K.; Kajdacsy-Balla, A.; Bagasra, O.; Costello, L. C. *Mol. Cancer* **2005**, *4*, 32−32.
(11) Feng, L.; Wang, J.; Li, H.; Luo, X.; Li, J. *Anal. Chim. Acta* **2017**, *984*, 66−75.
(12) González de Vega, R.; Fernández-Sanchez, M. L.; Eiro, N.; Vizoso, F. J.; Sperling, M.; Karst, U.; Sanz Medel, A. *Anal. Bioanal. Chem.* **2018**, *410* (3), 913−922.
(13) Bishop, D. P.; Clases, D.; Fryer, F.; Williams, E.; Wilkins, S.; Hare, D. J.; Cole, N.; Karst, U.; Doble, P. A. *J. Anal. At. Spectrom.* **2016**, *31* (1), 197−202.
(14) Arentz, G.; Mittal, P.; Zhang, C.; Ho, Y. Y.; Briggs, M.; Winderbaum, L.; Hoffmann, M. K.; Hoffmann, P. *Adv. Cancer Res.* **2017**, *134*, 27−66.
(15) Hou, J.; Chen, S.; Zhang, N.; Liu, H.; Wang, J.; He, Q.; Wang, J.; Xiong, S.; Nie, Z. *Analyst* **2014**, *139* (13), 3469−3475.
(16) Bertilsson, H.; Angelsen, A.; Viset, T.; Skogseth, H.; Tessem, M. B.; Halgunset, J. *Prostate* **2011**, *71* (5), 461−469.
(17) Nelson, K. A.; Daniels, G. J.; Fournie, J. W.; Hemmer, M. J. *J. Biomol Tech* **2013**, *24* (3), 119−127.
(18) He, L.; Diedrich, J.; Chu, Y.-Y.; Yates, J. R. *Anal. Chem.* **2015**, *87* (22), 11361−11367.
(19) Eijkel, G. B.; Kükrer Kaletaş, B.; van der Wiel, I. M.; Kros, J. M.; Luider, T. M.; Heeren, R. M. A. *Surf. Interface Anal.* **2009**, *41* (8), 675−685.
(20) Ellis, S. R.; Paine, M. R. L.; Eijkel, G. B.; Pauling, J. K.; Husen, P.; Jervelund, M. W.; Hermansson, M.; Ejsing, C. S.; Heeren, R. M. A. *Nat. Methods* **2018**, *15* (7), 515−518.
(21) Smith, C. A.; O'Maille, G.; Want, E. J.; Qin, C.; Trauger, S. A.; Brandon, T. R.; Custodio, D. E.; Abagyan, R.; Siuzdak, G. *Ther. Drug Monit.* **2005**, *27* (6), 747−751.
(22) Wishart, D. S.; Feunang, Y. D.; Marcu, A.; Guo, A. C.; Liang, K.; Vazquez-Fresno, R.; Sajed, T.; Johnson, D.; Li, C.; Karu, N.; Sayeeda, Z.; Lo, E.; Assempour, N.; Berjanskii, M.; Singhal, S.; Arndt, D.; Liang, Y.; Badran, H.; Grant, J.; Serra-Cayuela, A.; Liu, Y.; Mandal, R.; Neveu, V.; Pon, A.; Knox, C.; Wilson, M.; Manach, C.; Scalbert, A. *Nucleic Acids Res.* **2018**, *46* (D1), D608−d617.
(23) Patiny, L.; Borel, A. *J. Chem. Inf. Model.* **2013**, *53* (5), 1223−8.
(24) Revelle, W. R. *psych: Procedures for Personality and Psychological Research*, 2019.
(25) Wei, T.; Simko, V.; Levy, M.; Xie, Y.; Jin, Y.; Zemla, J. *Statistician* **2017**, *56*, 316−324.
(26) Pinheiro, J.; Bates, D.; DebRoy, S.; Sarkar, D.; R Core Team. *nlme: linear and nonlinear mixed effects models*, version 3.1−117; 2014. See http://CRAN.R-project.org/package=nlme.
(27) Cassese, A.; Ellis, S. R.; Ogrinc Potocnik, N.; Burgermeister, E.; Ebert, M.; Walch, A.; van den Maagdenberg, A. M.; McDonnell, L. A.; Heeren, R. M.; Balluff, B. *Anal. Chem.* **2016**, *88* (11), 5871−8.
(28) Hsiu, S.-I.; Huang, J.-F.; Sun, I. W.; Yuan, C.-H.; Shiea, J. *Electrochim. Acta* **2002**, *47* (27), 4367−4372.
(29) Chen, X.; Guo, H.; Abdeltawab, A. A.; Guan, Y.; Al-Deyab, S. S.; Yu, G.; Yu, L. *Energy Fuels* **2015**, *29* (5), 2998−3003.
(30) Koszinowski, K.; Böhrer, P. *Organometallics* **2009**, *28* (3), 771−779.
(31) Franklin, R. B.; Zou, J.; Yu, Z.; Costello, L. C. *BMC Biochem.* **2006**, *7*, 10−10.
(32) Selnaes, K. M.; Gribbestad, I. S.; Bertilsson, H.; Wright, A.; Angelsen, A.; Heerschap, A.; Tessem, M. B. *NMR Biomed.* **2013**, *26* (5), 600−6.
(33) Zand, B.; Previs, R. A.; Zacharias, N. M.; Rupaimoole, R.; Mitamura, T.; Nagaraja, A. S.; Guindani, M.; Dalton, H. J.; Yang, L.; Baddour, J.; Achreja, A.; Hu, W.; Pecot, C. V.; Ivan, C.; Wu, S. Y.; McCullough, C. R.; Gharpure, K. M.; Shoshan, E.; Pradeep, S.; Mangala, L. S.; Rodriguez-Aguayo, C.; Wang, Y.; Nick, A. M.; Davies, M. A.; Armaiz-Pena, G.; Liu, J.; Lutgendorf, S. K.; Baggerly, K. A.; Eli, M. B.; Lopez-Berestein, G.; Nagrath, D.; Bhattacharya, P. K.; Sood, A. K. *J. Natl. Cancer Inst.* **2016**, *108* (6), No. djv426.
(34) Lou, T. F.; Sethuraman, D.; Dospoy, P.; Srivastva, P.; Kim, H. S.; Kim, J.; Ma, X.; Chen, P. H.; Huffman, K. E.; Frink, R. E.; Larsen, J. E.; Lewis, C.; Um, S. W.; Kim, D. H.; Ahn, J. M.; DeBerardinis, R. J.; White, M. A.; Minna, J. D.; Yoo, H. *Cancer Prev. Res.* **2016**, *9* (1), 43−52.
(35) Shuster, J. R.; Lance, R. S.; Troyer, D. A. *BMC Clin. Pathol.* **2011**, *11*, 14.
(36) Bogner-Strauss, J. G. *Front. Endocrinol. (Lausanne, Switz.)* **2017**, *8*, 240.
(37) Suburu, J.; Chen, Y. Q. *Prostaglandins Other Lipid Mediators* **2012**, *98* (1−2), 1−10.
(38) Stewart, T. J. *Metallomics* **2019**, *11* (1), 29−49.
(39) Gumulec, J.; Masarik, M.; Adam, V.; Eckschlager, T.; Provaznik, I.; Kizek, R. *PLoS One* **2014**, *9* (6), No. e99790.
(40) Costello, L. C.; Franklin, R. B. *Mol. Cancer* **2006**, *5* (1), 17.
(41) Vaysse, P. M.; Heeren, R. M. A.; Porta, T.; Balluff, B. *Analyst* **2017**, *142* (15), 2690−2712.
(42) Ogrinc Potocnik, N.; Porta, T.; Becker, M.; Heeren, R. M.; Ellis, S. R. *Rapid Commun. Mass Spectrom.* **2015**, *29* (23), 2195−203.

https://dx.doi.org/10.1021/acs.analchem.9b04903
Anal. Chem. 2020, 92, 3171−3179